Paper ID: ETC2017-318

Proceedings of 12th European Conference on Turbomachinery Fluid dynamics
& Thermodynamics ETC12, April 3-7, 2017; Stockholm, Sweden

LARGE EDDY SIMULATION OF A LOW PRESSURE COMPRESSOR CASCADE AT HIGH INCIDENCE

J-S. Cagnone, M. Rasquin and K. Hillewaert

Cenaero, Gosselies, Belgium.

S. Hiernaux

Safran Aero Boosters, Liege, Belgium.

ABSTRACT

This work presents Large Eddy Simulations of a low pressure compressor cascade in order to understand the sudden rise of losses at high incidence. The simulation reveals a leading-edge separation bubble interacting with a superposed supersonic pocket ending in a normal shockwave. The unsteady interaction between the shear-layer and the shock is observed to be the principal transition mechanism. Through refinement studies, adequate mesh independence is demonstrated. The influence of turbulence injection at the inlet is also explored, and shown not to significantly alter the physics, although reducing the extent of the separation bubble.

NOMENCLATURE

C	Chord
L_f	Turbulence integral length scale
M	Mach number
P_0	Stagnation pressure
T_0	Stagnation temperature
Re	Reynolds number
$\Delta x^+, \Delta y^+, \Delta z^+$	Nondimensional mesh spacing
V	Velocity
μ	Dynamic viscosity
ρ	Density

INTRODUCTION

In this paper, we consider a cascade test bench at the von Karman Institute in collaboration with Safran Aero Boosters, designed to study the variation of the flow and loss mechanisms as a function of the solidity. The cascade consists of a fully prismatic blade, with the aim of reproducing (nearly) two-dimensional flow at midspan. A rapid increase of the losses at high incidence was measured, which could not be captured by accompanying RANS simulations which indicated a smooth, almost quadratic increase of the loss up to much higher incidences (Sans et al., 2015).

In order to understand the physics, Large Eddy Simulations are undertaken at high incidence using a 4th order accurate unstructured discontinuous Galerkin solver. In contrast to the RANS simulations, the endwalls were not taken into account to reduce the computational cost. Instead a spanwise periodic domain is used, corresponding to 10% of the axial chord. The objective of the study are three-fold. First of all, we aim at providing a detailed description of the flow physics, and gaining insight into the mechanism responsible for the increase in losses. Secondly, we demonstrate the mesh-independence of our simulation by systematically comparing two grid resolutions. Lastly, we probe into the effect of synthetic turbulence injected at the inlet, and observe its impact on the flow physics.

The remainder of the paper is organized as follows. The first section provides an overview of the case, together with the description of the flow regime. The second section explains our numerical methodology, and details the meshing strategy employed. The third section contains a dissection of the results based on post-processing of the calculated flows. Finally, the last section summarizes the important conclusions drawn from the study.

TEST CASE DESCRIPTION

The flow is assumed to be pitch-wise periodic, and the computations are therefore performed for a single blade only. Futhermore, we also assumed the flow to be nominally two-dimensional and only considered a fraction of the full blade height, supplemented by span-wise periodic boundary conditions. In the current computations, the extent of the span was fixed at 10%C, with a verification performed at 20%C.

The experimental Reynolds number is $Re_2 = 320k$. The flow conditions at the inlet were specified in terms of Mach number $M_1 = 0.5959$, total temperature and incidence angle (10.2°). Directly imposing these quantities proved unstable, and therefore, total conditions were imposed. Subsequently the inlet total pressure p_{01} was adjusted to obtain the correct inlet Mach number. This resulted in a slight increase of the Reynolds number to $Re_2 = 343.000$. This adjustment was performed for one computation; the obtained conditions were applied subsequently to all following computations. The (small) difference in Reynolds number can be attributed to the difference in losses due to the absence of the end walls in the computation.

The measured experimental inflow turbulence is specified by its intensity $T.I. \approx 1\%$ and its integral length scale L_f [1]. The measured value is surprisingly small, about 1/400 of the pitch. Sensitivity analysis on free stream turbulence decay indicate that at least one mesh cell[2] is required per integral length scale in order to properly resolve the turbulence. Resolving for the measured value would result in a very fine discretization, thus implying uniformly-fine resolutions even away from the body, corresponding to a boundary layer resolution near DNS (n^+ and t^+ in the order of unity). To mitigate this constraint, the sensitivity to inflow turbulence is instead studied by taking two extreme conditions. The first computations do not consider inflow turbulence, while the second set of calculations consider a higher integral length scale, which is 5 times higher than the initial specification, leading to reduced dissipation, and therefore a higher intensity at the blade. The comparison of both computations permit the analysis of at least the sensitivity to this parameter.

NUMERICAL METHODOLOGY

The computations are undertaken using a 4th order accurate discontinuous Galerkin discretization, using an implicit LES approach. The following subsections discuss the important features of the method in terms of spatial resolution, followed by the specification of the reso-

---

[1] The integral length scale L_f is defined as the integral of the longitudinal spatial correlation function $f(r)$, see (Batchelor, 1953).

[2] This corresponds to 4 degrees of freedom for the interpolation order p=3 used for this study; see section “Discontinuous Galerkin Method”.

lution used for the current study.

Discontinuous Galerkin Method

The discontinuous Galerkin method (DGM) (Cockburn, 1999; Arnold et al., 2002) is a finite element method based on a broken function space, composed of piecewise polynomial functions that are discontinuous across element interfaces. The solution state vector is approximated by a linear combinations of these functions within each element. The shape functions in Argo are Lagrange interpolants attached to interpolation points, which are defined independently for each element. This contrasts with continuous finite elements where nodes are shared by neighboring cells. The inter-element coupling is realized by exchanging fluxes, thereby ensuring local conservation and global energy stability. For the convective terms, approximate Riemann solvers (ARS) impose Dirichlet conditions following the incoming characteristics. The diffusive terms are discretised according to the Symmetric Interior Penalty (SIP) method (Arnold et al., 2002).

The method allows for an arbitrary order of interpolation p, which may be chosen independently for each element since no continuity of the interpolant is assumed. One can roughly assume that within each cell the interpolation uses $p + 1$ degrees of freedom in each direction. The order of convergence, measured in the L_2-norm of the solution, is $p + 1$. The polynomial allows for p zero crossings, such that the effective grid size or spectral resolution based on the Nyquist criterion is $h^* = h/p$, with h the characteristic grid size. Therefore the mesh size can be at least p times higher than that used for a finite volume computation. This is a conservative estimate since the higher order of accuracy will require fewer points to resolve a given flow feature.

Turbulence modeling approach

Within this study the *Implicit Large Eddy Simulations (iLES)* approach is used. This means that we rely on the numerical dissipation of the DG method to replace the subgrid scale model, which at first order should at least mimick the viscous dissipation occurring at the sub-grid scales. In most flow conditions, this turbulent dissipation is driven by inviscid mechanisms that transfer energy from large to small structures. In this case, the actual level of numerical dissipation is not important as it suffices to destroy the smallest structures at the rate they are created. The ILES method is continuously validated at Cenaero, and provides very good results on academic benchmarks of increasing complexity, including the Taylor-Green vortex (Carton de Wiart et al., 2013), homogeneous turbulence and channel flow (Carton de Wiart et al., 2014), the periodic hill case, and transonic turbulence (Hillewaert et al., 2016).

Turbulence injection

Finally, our modeling approach is complemented by a synthetic turbulence injection scheme following (Davidson, 2007). The method consists of perturbing the total inlet condition with pseudo-random velocity fluctuations v' of prescribed length scale and energy spectrum. Including turbulence injection with a total condition however requires some care.

For a clean inlet, the imposed flow velocity $\mathbf{v}^*$ is determined using the extrapolated norm of the velocity $||\mathbf{v}||$ as $\mathbf{v}^* = ||\mathbf{v}|| \, \mathbf{d}^*$. The imposed temperature T^* and pressure p^* are then found from the total temperature T_0^* and p_0^* as:

$$T^* = T_0^* - \frac{||\mathbf{v}^*||^2}{2C_p} \tag{1}$$

For the turbulent inlet, the imposed flow velocity is composed of a time-average value aligned with the imposed flow direction, superimposed by the velocity fluctuation $\mathbf{v}'$. Using the time-averaged value of the velocity $\bar{\mathbf{v}}$, the imposed velocity is computed as:

$$\mathbf{v}^* = ||\bar{\mathbf{v}}||\ \mathbf{d}^* + \mathbf{v}' \tag{2}$$

The full velocity needs to be taken into account when computing static pressure and temperature following equation 1, otherwise the additional turbulent kinetic energy will result in higher effective time-averaged values of the total pressure and temperature.

Meshes

Two mesh resolutions, referred to as the *coarse* and *nominal* grids, were selected for this study. These resolution are suitable for an interpolation order $p = 3$, leading to a 4th order accurate discretisation. Figure 1 displays the *coarse* grid. The meshes are constructed by the spanwise extrusion of a 2D unstructured quadrilateral mesh, and includes a structured boundary layer elements around the profile, as well as refinement boxes in the wake. Both mesh size and interpolation order are rapidly coarsened towards the exit, in order to damp outgoing structures before they interact with the outlet boundary condition and generate spurious acoustic waves.

The non-dimensional target wall normal spacing Δn^+ in the boundary layer[3] is $\Delta n^+ \approx 4$. This corresponds to an effective resolution of $\Delta n^+_{\text{eff}} = \Delta n^+/p \approx 1.3$ due to the internal degrees of freedom in the element. The streamwise spacing is then chosen to be about $\Delta s^+ = 300$ and $\Delta x^+ = 150$ for the *coarse* and *nominal* grids, respectively, corresponding to an effective resolutions of 100 and 50 respectively.

In the spanwise direction, the meshes are extruded over a total distance of 10% of the chord, using equispaced layers. A coarse mesh with a 20% extrusion was also considered to evaluate the sensitivity of the results to the spanwise periodic extent. Usually a higher resolution in the spanwise direction is used for DNS or LES of turbulent boundary layers. However in transitional, separation and reattachment regions typically much more isotropic flow features are observed than in the developed boundary layer. The interaction of the unsteady shock system separation with the boundary layer even results in flow structures which are richer in the stream- than in the spanwise direction. As the location of these phenomena is not known a priori, an isotropic grid resolution in the near-wall turbulent regions has been ensured on the whole profile.

Finally, two additional grids tailored to inflow turbulence were also constructed. These grids retain the mesh spacings previously described, but also feature 80 elements along the length of the inlet. This increased inlet resolution was chosen to fullfill the best-practice guideline of providing at least one element per integral length L_f.

Time integration strategy

LES calculations in Argo are marched in time using the second-order backward-difference formula (BDF2). At each time-step, a non-linear system is solved using Newton's method. The resulting linear system is solved using a matrix-free implementation of the GMRES algorithm. The preconditioner is formed by neglecting the off-diagonal matrix entries, leading to a simple and efficient block-Jacobi strategy.

---

[3] Wall spacing are specified in wall-units, *i.e.* non-dimensionalized using the wall shear stress τ: $\Delta n^+ = \rho \Delta n u_\tau / \mu$, with $u_\tau = \sqrt{\tau/\rho}$.

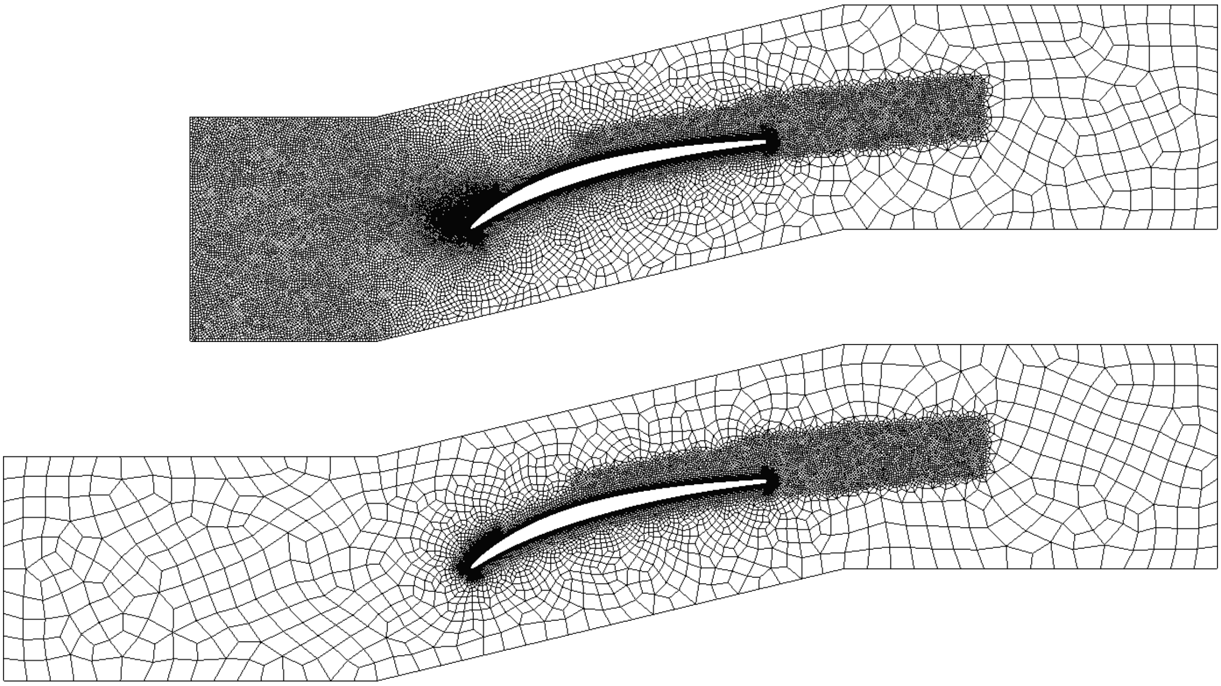

Figure 1: Nominal mesh resolution for computations without and with inlet turbulence.

	Nb Elements	Dof/variable	Ratio
Coarse, 10% span	68,679	4,395,456	1.0
Coarse, 20% Span	137,358	8,790,912	2.0
Coarse, 10% span, inflow turbulence	222,456	14,237,184	3.2
Nominal, 10% span	380,276	24,337,664	5.5
Nominal, 10% span, inflow turbulence	740,844	47,414,016	10.8

Table 1: Summary of the computational meshes.

This implicit formulation allows to select the time-step based on the turbulence time-scale, rather than on the more restrictive acoustic or diffusive stability bounds. In our calculations, the time step was selected based on the inlet-flow velocity and the smallest element size, and corresponds to a CFL[4] number of 0.4 for the *coarse* and 0.8 for the *nominal* mesh.

Acquisition of statistical data and computational cost

The aquisition of the statistical data is performed in two phases. First, the simulation is run until a fully turbulent flow is established, and the inlet and outlet fluxes reach a stabilized value by checking the stationarity of the time averaged pressure distribution as well as the wake total pressure and flow angle profile. The flow statistics are then accumulated over five additional particle flow-through times. Statistical convergence is also enhanced by averaging the solution along the span-wise direction. For reference, this exercise took about 50 flow-through times for the first computations, which was started from a uniform flow. The later computations were started from the earlier obtained solutions.

---

[4] The CFL (Courant-Friedrichs-Lewy) number is defined as $\frac{U\Delta t}{h}$.

The computational cost varies from 16.000 seconds for the clean inlet coarse computation to 73.000 seconds for the turbulent inflow computations on the nominal mesh, per particle flow-through time.

CLEAN INFLOW RESULTS

This section details the instantaneous and time-averaged results obtained for the simulation without inflow turbulence. A general overview of the flow topology is illustrated in Fig. 2, showing the spanwise component of vorticity on the periodic plane. We see that the flow is dominated by a very thick, large scale turbulent boundary layer. On the pressure side the flow remains mainly laminar due to the continuously favorable pressure gradient. A more detailed visualization comparing the instantaneous and time-averaged flow past the leading-edge is shown in Fig. 3. A supersonic region is discerned, ending abruptly in a normal shockwave. The flow furthermore features a laminar separation at the leading edge, resulting in a separation bubble underneath the supersonic region. The interaction of the shear layer and the normal shock wave is highly unsteady and threedimensional, resulting in transition and production of turbulent structures which develop into the turbulent boundary layer downstream. The separation bubble itself is initially laminar but is regularly perturbed by flow structures propagating upstream from the shock/boundary layer interaction region. Interestingly, the shockwave is smeared by the time-averaging procedure, and does not appear in the mean flow field of Fig. 3b. This partly explains why steady RANS calculations, missing the principal turbulence-generation mechanism, yielded unsatisfactory loss predictions.

Figure 4 offers a three-dimensional view of the leading-edge flow. Above the shear layer, the flow is supersonic so no structures can move upstream, whereas underneath the shear layer turbulent flow features are seen to move from the shock towards the leading edge. The bidimensional undulation of the Mach isocontour near the leading edge is not explained, but it is not stationary and apparently not related to the mesh resolution. We suspect this to be the result of the reflections and trapping of acoustic waves, and this feature should be further investigated.

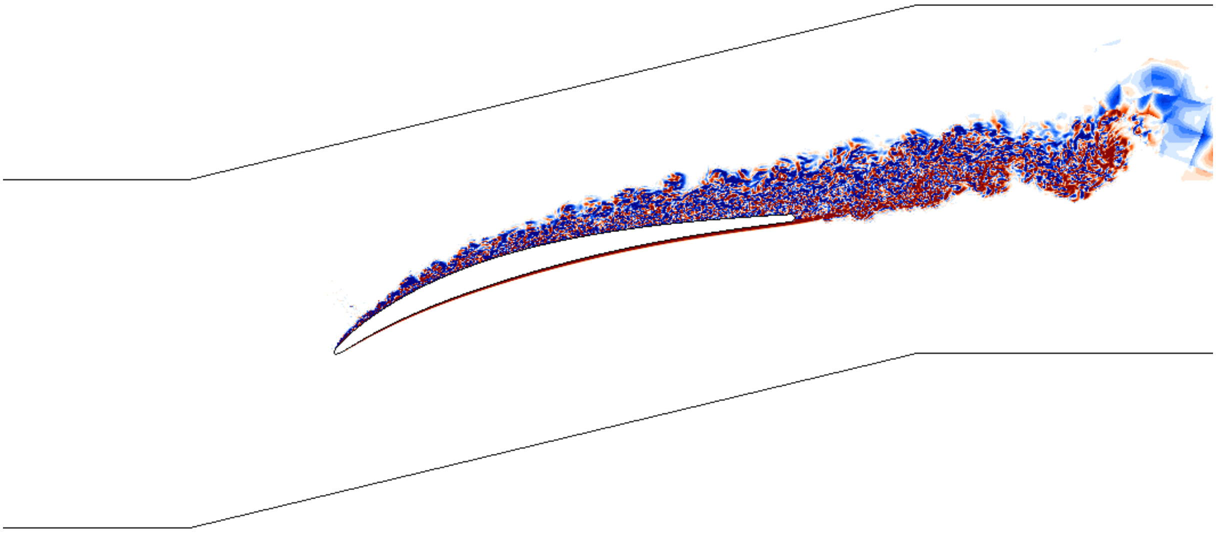

Figure 2: Instantaneous spanwise vorticity contours computed on the *Nominal* mesh without inflow turbulence.

Figure 5 compares the time-averaged isentropic Mach number distribution on the blade, as

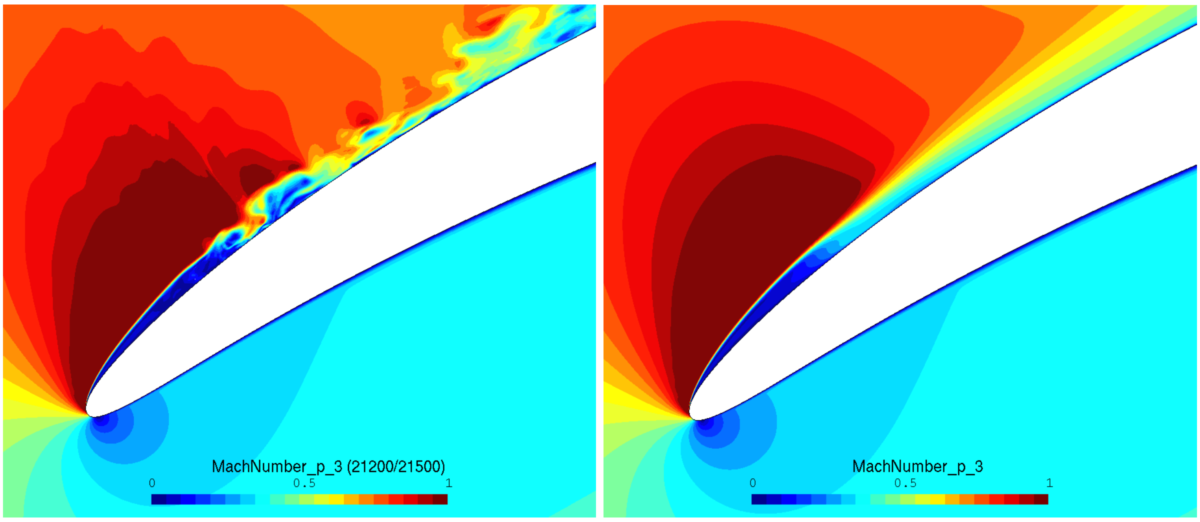

(a) Instantaneous (b) Time-Averaged

Figure 3: Mach number contours for the computations without inflow turbulence. Contours are shown every 0.05, and are saturated at M=1.

	Loss coefficient	Flow angle [deg]
Coarse	0.1023	10.02°
Nominal	0.1038	10.41°
Coarse 20%	0.1078	9.65°
Coarse, inflow turbulence	0.1006	10.00°
Nominal, inflow turbulence	0.0964	10.42°
Tunnel	0.1337	8.89°
RANS	0.03	-

Table 2: Integrated wake losses and outlet flow angles

well as the variation of losses and flow angle across the wake at the experimental measurement location, *i.e.* 48.28 [mm] downstream of the leading edge. The pressure plateau caused by the separation bubble, and the rapid recompression past the shock is clearly identifiable at the 10% chord location. The data obtained on the *coarse* and *nominal* mesh are in close agreement, confirming these results are largely mesh independent. The difference is most marked in a small but global shift of the flow turning angle ($\approx 0.5°$). As the inlet conditions were kept constant, the latter is probably due to the slight differences in losses, which then translates in a change of the mass flow. An analogous verification was performed by increasing the span of the domain to 20%C. Although not shown here, the time-averaged distribution were nearly unchanged, indicating that span extent of 10% is sufficient.

Finally, table 2 summarizes the integrated total-pressure losses[5] and outlet flow angles for the different cases presented so far. All three LES results are in close agreement, and compare well to the experimental values. As previously explained, the RANS calculations were unable to capture the upper-surface turbulence, and thus underpredict the integrated loss coefficient.

---

[5] Computed as $\frac{P_{01}-\overline{P_0}}{P_{01}-P_2}$, where $\overline{P_0}$ denotes the mean total-pressure integrated over the measurement plane.

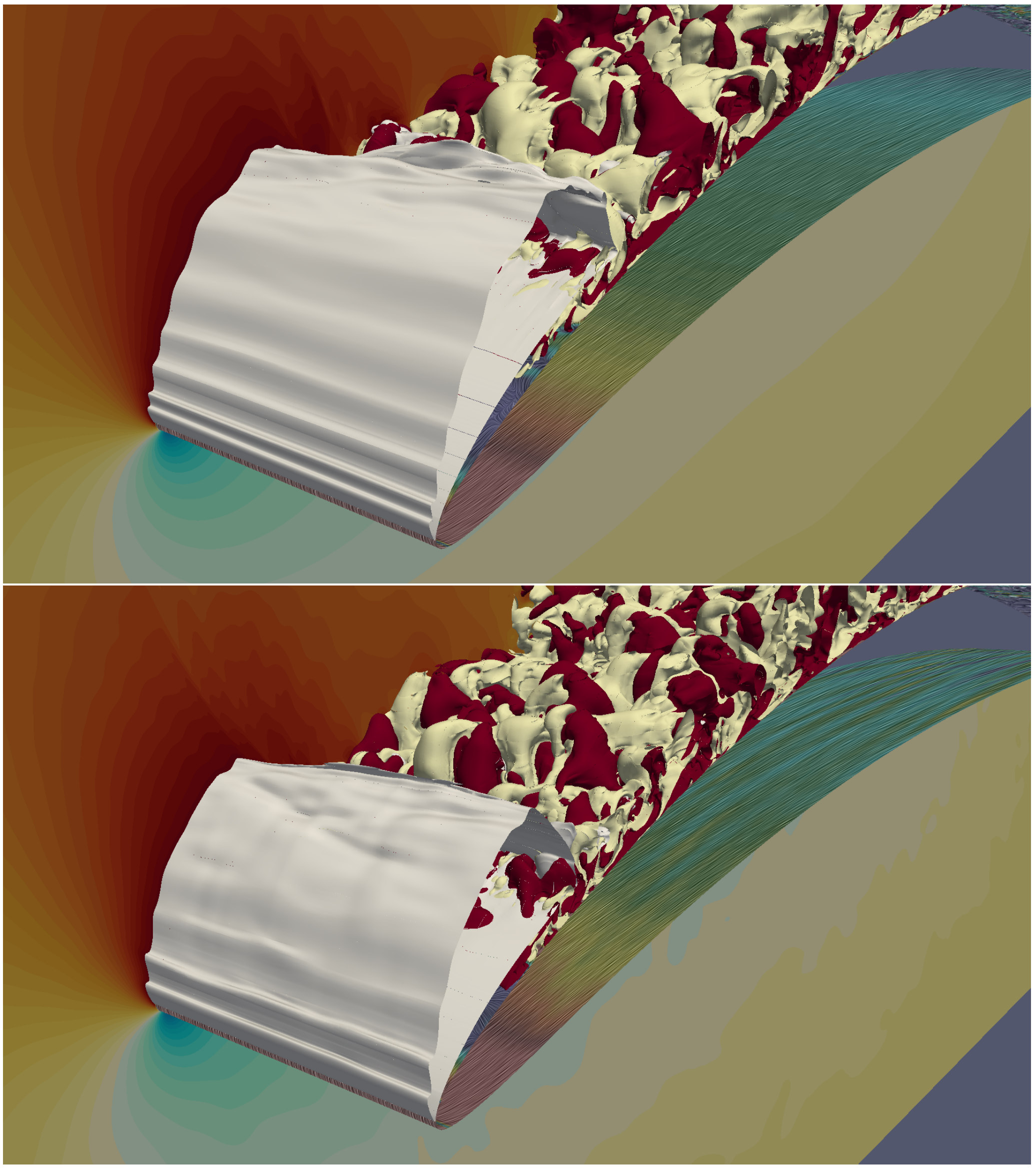

Figure 4: Isocontours of positive and negative transverse velocity v_z and isocontour $M = 1$ without and with inflow turbulence.

TURBULENT INFLOW RESULTS

This section describes the calculations including inflow turbulence. Figure 6 presents the contours of the instantaneous spanwise component of the vorticity. Similarly to the results without inflow turbulence, we observe a highly turbulent zone on the upper-surface of the airfoil. However, the last 20% of the pressure side surface now displays turbulent structures, which contrasts with the previous calculation where the same boundary layer remained fully laminar.

Figure 7 compares the time-averaged flow near the leading edge. We see that the inflow turbulence reduces the leading edge recirculation region. Figure 8 shows the time-averaged profiles of isentropic Mach distribution, wake losses and outlet flow angle. Observing the Mach distribution, we see that the main impact of the inflow-turbulence is on the leading-edge peak Mach number, which is higher for the latter simulation. This increase is consistent with the smaller laminar separation bubble, whose reduced displacement-thickness imposes an larger

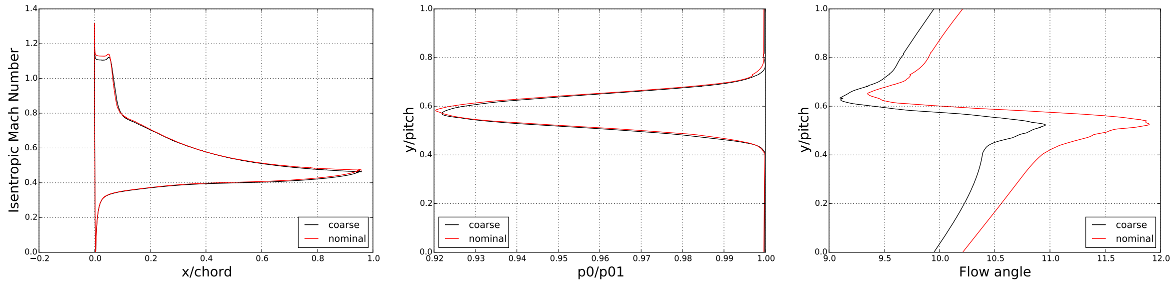

Figure 5: Time-averaged distributions of the isentropic Mach number on the blade as well as the relative total pressure loss and flow angle across the wake for the *coarse* and *nominal* meshes without inflow turbulence.

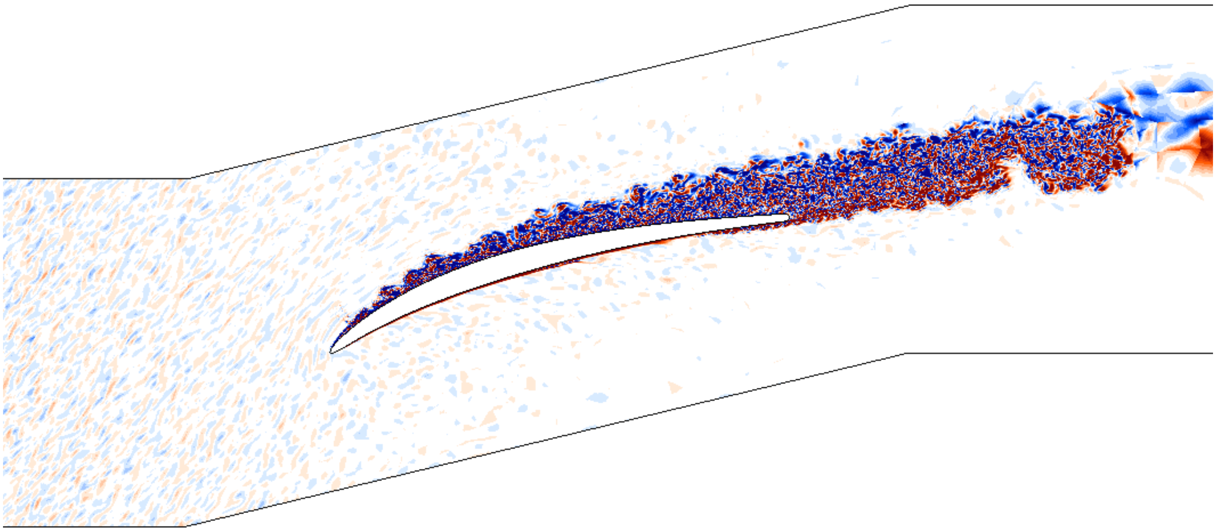

Figure 6: Contours of the instantaneous spanwise vorticity computed on the *nominal* mesh with inflow turbulence.

acceleration of the high-incidence flow around the leading edge. Turning our attention to the wake losses and outlet flow angles, we observe only minor differences with respect to the calculations without inflow turbulence. We note that the addition of inflow turbulence reduces slightly the wake losses, and has a small effect on the outflow angle. The integrated wake losses and outlet flow angle, reported in table 2, also confirm that these quantities are only slightly influenced by the turbulence injection.

CONCLUSIONS

This paper presented the first findings of the LES calculations of a low pressure compressor blade at moderate Reynolds number in order to understand a rapid increase in loss with inlet angle, which was not predicted using RANS. Whereas the paper focuses on illustrating the physics of the flow, future work will be directed to studying more flow conditions, and performing a more detailed quantitative analysis, *a.o.* of the loss mechanisms.

Visualisations of the flow field revealed a leading-edge supersonic pocket, on top of a laminar separation bubble. The latter provides an apparent change in geometry, leading to an enhanced flow acceleration. The supersonic pocket is closed by a three-dimensional unsteady

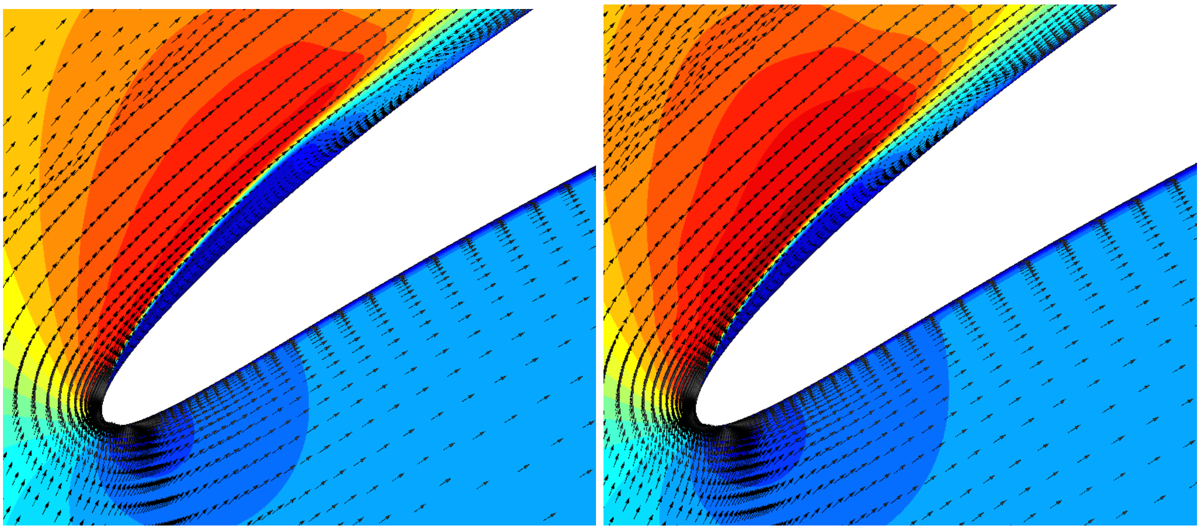

(a) Without inflow turbulence.

(b) With inflow turbulence.

Figure 7: Comparison of time-averaged Mach contours and velocity vectors for the computations with and without inflow turbulence, obtained on the *nominal* meshes. Contours are shown every 0.05, and are again saturated at M=1.

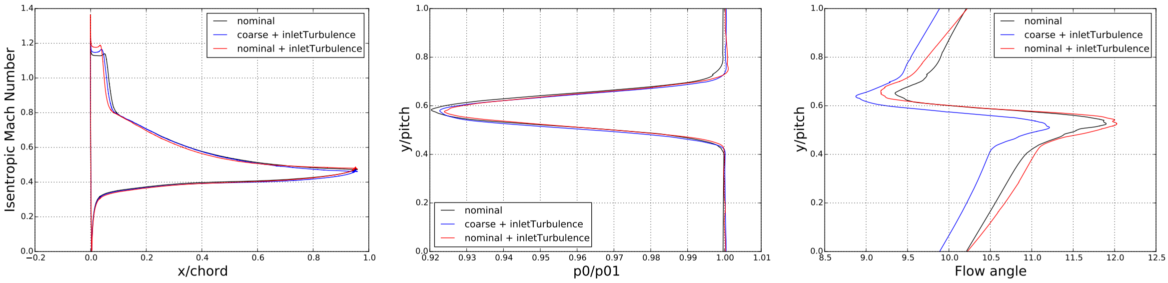

Figure 8: Time-averaged distributions of the isentropic Mach number on the blade as well as the relative total pressure loss and flow angle across the wake, comparing computations with and without inflow turbulence.

shock system, which overlaps with the reattachment and transition region. This unsteady interaction results in transition and production of turbulent structures which develop into a thick highly-turbulent boundary layer. Although the instantaneous (multiple) shocks are sharp, a single diffuse shock is apparent in the time-averaged Mach number distribution. We conjecture that this subtle transition mechanism is not accounted for in RANS models, which did not capture the separation and the ensuing thick boundary layer. In any case, a good agreement of the loss and flow angle are reported here, despite the assumption of spanwise periodicity.

Studies were undertaken without and with inlet turbulence, showing very similar physics with only minor differences. The inlet turbulence tends to reduces the size of the combined system of recirculation region and supersonic pocket, and triggers transition on the last 20%C of the pressure-side.

As far as we are aware, no work has been dedicated to integrating this specific flow phenomenon into a transition model. This would however in theory be required to improve RANS prediction for this particular case. As a second consequence is that the (tolerance on the) leading edge shape is probably more critical for these off-design conditions than previously assumed.

ACKNOWLEDGEMENTS

Part of the Argo computations were performed using computational resources made available on the Tier-1 supercomputer of the Fédération Wallonie-Bruxelles, infrastructure funded by the Walloon Region under the grant agreement n°1117545.

References

D.N. Arnold, F. Brezzi, B. Cockburn, and L.D. Marini. Unified Analysis of Discontinuous Galerkin Methods for Elliptic Problems. *SIAM Journal of Numerical Analysis*, 39:1749–1779, 2002.

G.K. Batchelor. *The Theory of Homogeneous Turbulence*. Cambridge Science Classics. Cambridge University Press, 1953. ISBN 9780521041171. URL `https://books.google.be/books?id=POG-LSUgYckC`.

C. Carton de Wiart, K. Hillewaert, M. Duponcheel, and G. Winckelmans. Assessment of a discontinuous Galerkin method for the simulation of vortical flows at high Reynolds number. *Int. J. Numer. Meth. Fluids*, 74:469–493, 2013. doi: 10.1002/fld.3859.

C. Carton de Wiart, K. Hillewaert, L. Bricteux, and G. Winckelmans. Implicit LES of free and wall bounded turbulent flows based on the discontinuous Galerkin/symmetric interior penalty method. *International Journal of Numerical Methods in Fluids*, 78(6):335–354, 11 March 2014. doi 10.1002/fld.4021.

B. Cockburn. *Higher-Order Methods for Computational Physics*, volume 9 of *Lecture Notes in Computational Science and Engineering*, chapter Discontinuous Galerkin Methods for Convection-Dominated Problems, pages 69–224. Springer, 1999.

L. Davidson. Using isotropic synthetic fluctuations as inlet boundary conditions for unsteady simulations. *Advances and Applications in Fluid Mechanics*, 1:1–35, 2007.

K. Hillewaert, J.S. Cagnone, S. Murman, A. Garai, L. Yu, and M. Ihme. Assessement of high order DG methods for LES of free stream transonic turbulence. In *Proceedings of the summer program 2016*. Center for turbulence research, Stanford University, 2016.

J. Sans, J.-F. Brouckaert, and S. Hiernaux. Experimental and numerical investigations of the solidity effect on a linear compressor cascade. In *Turbo Expo: Turbine Technical Conference and Exposition*, Montreal, Quebec, June 15-19 2015. ASME.